JOURNAL OF GUIDANCE, CONTROL, AND DYNAMICS
Vol. 31, No. 3, May–June 2008

Propellant-Free Control of Tethered Formation Flight, Part 1: Linear Control and Experimentation

Soon-Jo Chung*
Iowa State University, Ames, Iowa 50011
and
David W. Miller†
Massachusetts Institute of Technology,
Cambridge, Massachusetts 02139

DOI: 10.2514/1.32188

We introduce a decentralized attitude control strategy that can dramatically reduce the usage of propellant, by taking full advantage of the physical coupling of the tether. Motivated by a controllability analysis, indicating that both array resizing and spin-up are fully controllable by the reaction wheels and the tether motor, we report the first propellant-free underactuated control results for tethered formation flying spacecraft. This paper also describes the hardware development and experimental validation of the proposed method using the Synchronized Position Hold, Engage, and Reorient Experimental Satellites test bed. In particular, a new relative sensing mechanism that uses six-degree-of-freedom force-torque sensors and rate gyroscopes is introduced and validated in the closed-loop control experiments.

I. Introduction

NASA's Submillimeter Probe of the Evolution of Cosmic Structure (SPECS) mission [1–5] is proposed as a tethered-spacecraft interferometer (TSI) that detects submillimeter-wavelength light from the early universe. The kinds of stellar objects that will be observed will contain information at many spatial frequencies, thus the ability of interferometers to observe at multiple baselines will be key. Tethered formation flight enables interferometric baseline changes with minimal fuel consumption; without tethers, a massive amount of fuel would be required to power the thrusters to change the baseline, as in the a separated spacecraft interferometer (SSI) architecture.

The basic observation scenario is to reel the tethers out or in gradually while rotating the array in a plane perpendicular to the target being observed (see Figs. 1 and 2). Compared to free-flying separated formation flight, tethered formation flight is a more efficient way to both control the spacecraft and to know their relative positions: multidirectional force measurements at the tether attachment points can be used to determine the relative attitude, as shown in Sec. IV. Figure 1 illustrates a potential mission scenario of the deployment and retrieval operation. A completely docked, tethered-spacecraft array is released from a mother spaceship (see Fig. 1a). The docked spacecraft are initially at zero speed, and spun to reach some target angular rate (see Fig. 1b). Then, the tether is deployed at a predefined speed to meet the UV coverage [6] requirement (see Figs. 1c and 1d). Once a tethered array spun by reaction wheels reaches its maximum size, a new momentum dumping method that does not need torque-generating thrusters [7] can be used to extend the size beyond this limit or the tether is retrieved to fill smaller spatial UV frequencies. Such a maneuver is experimentally validated in Sec. V.

One of several decisions, yet to be confirmed with respect to the future tethered formation flight missions, is the actuation method. This paper focuses on the method of spacecraft actuation to control the spin rate of the array as well as relative motions of each spacecraft. Another objective of this paper is to present closed-loop control experiments of tethered formation flight, which permit the verification of a system-level integration of various subsystems including actuators, sensors, and control algorithms. Because no previous space science mission has used a tethered formation flight architecture, control experimentation is indispensable to validate control/estimation algorithms, to verify simulation results, and to capture unmodeled physical phenomena.

It should be noted that the control of tethered-spacecraft will be responsible only for a fraction of the required precision. As a rule of thumb, controlling the locations of the apertures to within 10 cm is sufficient, whereas the fine staged optical control maintains the optical path-length difference (OPD) between individual apertures within a tenth of the operating wavelength [6]. A longer wavelength of the far-infrared/submillimeter (FIR/SMM) range makes SPECS even more technologically feasible: compare SPECS's wavelength range of 40–640 μm to 10–17 μm of the Terrestrial Planet Finder Interferometer (TPF-I) mission.

As stated earlier, accomplishing the goal of spiraling out and reaching some required level of UV plane coverage using the traditional thrusters leads to prohibitively high propellant usage. Beyond the fuel saving by employing tethered formation flight, this paper proposes a new actuation method, which further reduces the usage of propellant. In essence, we investigate the feasibility of controlling the array spin rate and relative attitude without thrusters. Such a tethered formation flight array without thrusters is characterized as an underactuated mechanical system. There are several advantages to the proposed underactuated control strategy. First, using reaction wheels instead of thrusters implies that power will be supplied via conversion of solar energy instead of carrying expensive propellant. We still envision using thrusters for out-of-plane motions [7], but the life span of the mission would be greatly increased by using reaction wheels for controlling the array spin rate. Second, the optics will not risk contamination by exhaust from the thrusters. The main application of tethered formation flight is stellar interferometry, and optics contamination should be avoided by all means.

Presented as Paper 6858 at the AIAA Guidance, Navigation, and Control Conference and Exhibit (GN&C), at the Marriott Hilton Head Beach and Golf Resort in Hilton Head, SC, 20–23 August 2007; received 16 May 2007; revision received 23 September 2007; accepted for publication 5 October 2007.

*Assistant Professor of Aerospace Engineering; sjchung@alum.mit.edu. AIAA Member.

†Professor, Department of Aeronautics and Astronautics; millerd@mit.edu. AIAA Senior Member.

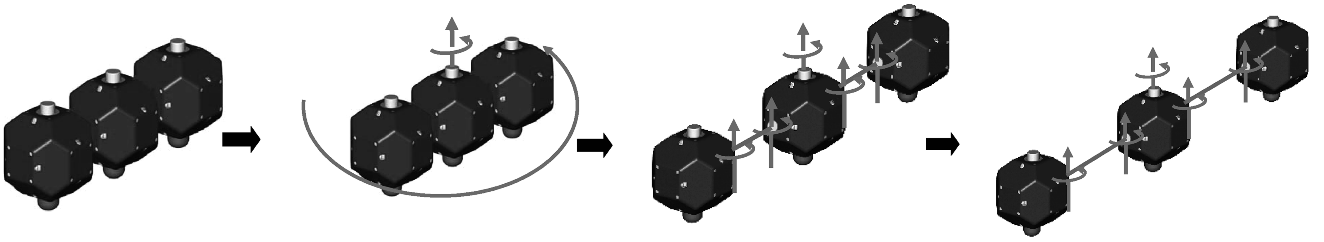

a) Prelaunch configuration. Just released from the mother spacecraft

b) Initial spin-up

c) Tether deployment

d) Operation at various tether lengths

Fig. 1 Deployment and operational maneuvers of tethered formation flight spacecraft.

The stability and controllability analysis, in conjunction with the compound pendulum modes of the tethered arrays, constitutes another contribution of this paper. In addition, the dynamics modeling in this article facilitates nonlinear spatial decoupling of multiple-spacecraft coupled arrays; the dynamics modeling in this paper permits a relative and decentralized sensing mechanism for deep space formation flight. In deep space, absolute attitude might be available via star-trackers but the availability of absolute positions, like those provided by the Global Positioning System (GPS), is very limited.

The decentralized control approach, first introduced in [8], is further generalized in this series of papers. The proposed method is unique in the sense that we use oscillation synchronization to simplify the coupled dynamics into the simplest form for which combined stability can be analyzed systematically (we refer the readers to [8] for further details). The importance of this approach lies with the fact that we can employ a fully decentralized control law (or estimation algorithm) from the reduced single-tether system to control a more complex multiple-spacecraft array, thereby reducing the complexity of both hardware and software. The decentralized controller will enable simple independent control of each satellite without the need for exchanging individual state information. This will significantly simplify both the control algorithm and hardware implementation, as well as eliminating the possibility of performance degradation due to noisy and delayed communications.

Tethered formation flight has been a popular area of research. An extensive literature survey can be found in a very recent paper [9] as well as in a newly published book [10]. Some papers investigated dynamics and control of tethered formation flying, particularly tailored toward the SPECS mission [1–5]. Previous work on tethered satellite formation flight is based upon the assumption that the tethered system is fully actuated, whereas this article deals with underactuated tethered systems equipped with only reaction wheels. In addition, we pay particular attention to control of oscillations of the compound pendulum mode of tethered formation flight satellites. The representative work on tethered formation flight [11–16] does not include the compound pendulum mode, by assuming that the spacecraft can be regarded as a point mass with a long tether. However, the stability analysis in this paper shows that it is indispensable to examine this mode because of the instability occurring while retracting the tether in spinning arrays. Previously, the instability of the tether retrieval was usually discussed in the context of two point masses connected by a single tether [9].

Several space missions have already been flown to verify tethered satellite systems (TSS). These important milestones include NASA and Italian Space Agency's retrieval of tether in space (TSS-1 in 1992, TSS-1R in 1996), NASA's Small Expendable Deployer System (SEDS-1 in 1993, SEDS-2 in 1994), and the U.S. Naval Research Laboratory's tether physics and survivability (TiPS in 1996). Descriptions of these missions are found in the tether handbook [17]. The review paper [9] also introduces some ground-based experimental results of the out-of-plane libration control scheme with the equivalent tension control law with tether length and length rate as feedback [18], and active control of the in-plane pendulum oscillations and tether bobbling of the TSS by boom rotation [19].

To our knowledge, there exist only three closed-loop control experiments on tethered formation flight: work done by Stanford University [20–22], the three-spacecraft simulator by the Japanese research group [23,24], and the Massachusetts Institute of Technology (MIT) synchronized position hold, engage, and reorient experimental satellites (SPHERES) test bed introduced in this paper and [8]. A notable previous experiment using two-inline satellites is reported in [20]. The experimental hardware consists of two spacecraft modules that float on gas bearings on a granite table. A one-degree-of-freedom (DOF) potentiometer was employed to measure the relative angles between the spacecraft, in contrast with the six-DOF force-torque (F/T) sensor used for this article. A recent paper also describes the tethered-satellites test bed with a triangular configuration [23]. As opposed to the tethered system in [23], which relies on a global metrology system using a charge-coupled device (CCD) camera overlooking the array, this article proposes a new decentralized and relative sensing mechanism for tethered formation flight. The MIT SPHERES test bed, presented in this paper, is the first satellite test bed fully exploiting the dynamics of tethered satellites under various formation flight configurations including a two-inline, a three-inline, and a triangular configuration. It is also a fully three-dimensional operational satellite with sophisticated sensors and actuators, permitting replication of an operational mode representative of real world spacecraft. In other words, it could control in three dimensions.

The remainder of the paper is organized as follows. In Sec.II, we present the modeling and controllability analysis of tethered formation flight, with emphasis on model reduction and decoupling. We introduce the gain-scheduled linear quadratic regulator (LQR) control approach in Sec. III. In Sec. IV, we describe the SPHERES test bed. In particular, a relative metrology system that incorporates both the force-torque sensor and gyro measurements is introduced in Section IV.C. Finally, we discuss closed-loop control results in Sec. V.

II. Modeling and Controllability

Following the nonlinear equations of motion introduced in the recent paper [8], this section presents the linearized equations of planar motion of the tethered formation flying spacecraft considered in the entire paper. We also justify the proposed propellant-free control approach by conducting a controllability analysis.

A. Reduction of Three-Dimensional Dynamics to Planar Motion

The rationale behind the reduced dynamics modeling on the two-dimensional plane is that the symmetry of a spinning array can be exploited to decouple the in-plane rotational motions from the out-of-plane motions.

Figure 2 shows a three-spacecraft tethered array in the inline configuration. The simplified Euler's rotational equations of motion of the three identical spacecraft array at the center of mass of the spacecraft formation become

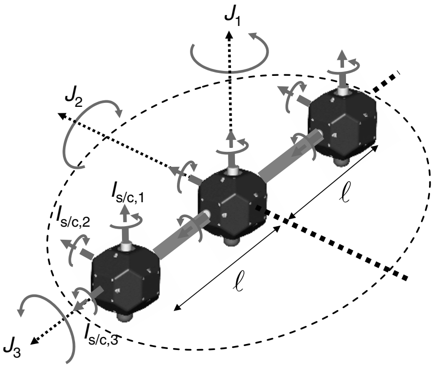

Fig. 2 Decoupling of the in-plane rotational motions from the out-of-plane motions justifies the proposed approach to reduce a three-dimensional attitude dynamics to a two-dimensional case.

$$\begin{bmatrix} J_1 & 0 & 0 \\ 0 & J_2 & 0 \\ 0 & 0 & J_3 \end{bmatrix}\begin{pmatrix} \dot{\omega}_1 \\ \dot{\omega}_2 \\ \dot{\omega}_3 \end{pmatrix} + \begin{bmatrix} 0 & -\omega_3 & \omega_2 \\ \omega_3 & 0 & -\omega_1 \\ -\omega_2 & \omega_1 & 0 \end{bmatrix}\begin{bmatrix} J_1 & 0 & 0 \\ 0 & J_2 & 0 \\ 0 & 0 & J_3 \end{bmatrix}\begin{pmatrix} \omega_1 \\ \omega_2 \\ \omega_3 \end{pmatrix} = \begin{pmatrix} \tau_1 \\ \tau_2 \\ \tau_3 \end{pmatrix} \tag{1}$$

where J_i with $i = 1, 2, 3$ is the moment of inertia of the tethered-spacecraft array in Fig. 2. This implies that $J_1 = I_{s/c,1} + 2(I_{s/c,1} + m\ell^2)$ for the vertical axis (axis 1), where $I_{s/c,1}$ denotes the moment of inertia of an individual spacecraft in the body frame, and ℓ is the radius of the array. For the second axis, J_2 is similarly defined as $J_2 = 3I_{s/c,2} + 2m\ell^2$.

For simplicity, let us assume that all relative angles between spacecraft are small (i.e., perfectly aligned). The first axis is perpendicular to the plane of rotation, defined by the second and third axes. Rotations about the second axis would characterize out-of-plane motions, whereas the third axis lies along the tethers. If the individual spacecraft are axisymmetric [25], such that $I_{s/c,1} = I_{s/c,2}$, then the spacecraft array is also axisymmetric about the tether line (axis 3), resulting in $J_1 = J_2 = J = 3I_{s/c,1} + 2m\ell^2 = 3I_{s/c,2} + 2m\ell^2$. Hence, Eq. (1) reduces to

$$J\dot{\omega}_1 - (J - J_3)\omega_3\omega_2 = \tau_1 \qquad J\dot{\omega}_2 - (J - J_3)\omega_3\omega_1 = \tau_2$$
$$J_3\dot{\omega}_3 = \tau_3 \tag{2}$$

which indicates that the dynamics of a torsional rotational rate ω_3 are completely decoupled from the other axes.

We can implement a simple control law τ_3 to regulate ω_3 and $\dot{\omega}_3$ to zero at all times. This further reduces the dynamics to

$$J\dot{\omega}_1 = \tau_1 \qquad J\dot{\omega}_2 = \tau_2 \tag{3}$$

which in turn corresponds to decoupling of the in-plane rotational dynamics (axis 1) from the out-of-plane motions (axis 2).

Note that a similar reduction can be carried out for arbitrarily large circular arrays of tethered spacecraft, including a three triangular configuration. As a result, out-of-plane motions can be separately controlled without affecting the rotational dynamics of the array. This result agrees with the previous result [9] in the sense that out-of-plane libration motion of the tethered array is generally small and has less effect on the rotational motion than the in-plane motion. In the remainder of this paper, we present the dynamics modeling and control experiment on this two-dimensional rotational plane (see Fig. 2).

B. Reduction to Single-Tethered Systems

It is proven in the previous paper [8] on model reduction of tethered formation flight that the hierarchical combination, inherent in the dynamics of a three-inline configuration in Fig. 2, reduces the dynamic model to two single-tethered systems shown in Fig. 3 if the center spacecraft becomes exponentially stabilized. Similarly, a two-spacecraft tethered array is shown to be the parallel combination of two single-tethered systems. This model reduction has been generalized for arbitrarily large circular arrays of tethered spacecraft [8]. This decoupling follows from the fact that implementing an underactuated control law, based on the single-tethered dynamics shown in Fig. 3, ensures the stability of multispacecraft tethered arrays. Therefore, we will first focus on the single-tethered system, and then move onto tethered arrays composed of multiple spacecraft in the subsequent sections.

Figure 3 shows a single satellite revolving about the center of the fixed inertial axes X–Y. The body-fixed axes x–y are chosen such that the y direction always coincides with the direction of increasing θ, whereas the x direction is aligned with the tether. The notation T is the tension force in the tether, F is the force due to thruster firing, and u is the torque exerted on the c.m. by a reaction wheel assembly (RWA).

The following assumptions are made. First, the tether is assumed to be ideal, i.e., massless and inextensible. Hence, neither longitudinal nor transverse vibrations of the tether are allowed. The zero mass assumption can be realized by rather strong thin material like Kevlar to avoid a detrimental phenomenon, such as the coupling between in-plane and out-of-plane oscillations of a more massive tether and the spacecraft attitude. At this point, the tether of SPECS consists of four tether lines, each with an oblate flattened cross section [5]. It is estimated that the total mass of the 1-km-long ribbon tether will be less than 30 kg. Second, the array is assumed to always rotate at a certain angular rate. As a result, the tether is taut and straight at all times. A nonzero angular rotation is a realistic assumption because tethered interferometers will attempt to provide a complete UV coverage by rotation. Third, for simplicity, the tether

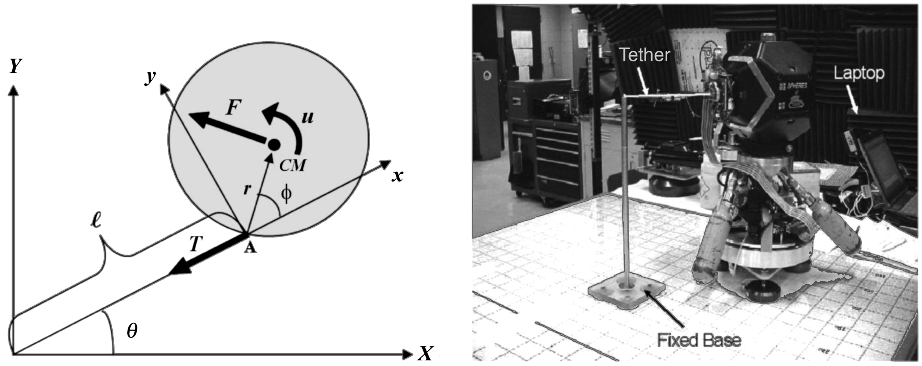

a) Free-body diagram of a spinning single-tethered SPHERES

b) Experimental setup using the SPHERES testbed

Fig. 3 Spinning single-tethered SPHERES.

reels in and out only at constant speed ($\dot{\ell} = \text{constant}$). The speed of the tether motor can be easily predefined in the control code and does not constitute one of the system states. This tether velocity control has been successfully validated with the SPHERES test bed, as shown in Sec. V. Last, the gravity term is neglected under the assumption that a tethered formation array such as SPECS will operate in a very weak gravity field, e.g. the second Lagrangian point L2 of the Earth–sun system. The operation of tethered formation arrays in any kind of Earth orbit is not plausible due to expensive fuel consumption and unsatisfactory photon yield [12]. Operating at L2 also offers other advantages. For instance, this allows the tethered flight to be relatively undisturbed by gravity gradients avoiding significant wobbling of a spinning array. In addition, the L2 point provides a relatively unobstructed view of the sky and a lower thermal radiation background than low-Earth orbit, which facilitates cryocooling. More important, the thermal environment is less variable with the sun remaining fixed with respect to the spacecraft. The L2 point is unstable on a time scale of approximately 23 days, which requires satellites parked at these positions to undergo regular course and attitude corrections. Controlwise, any additional unmodeled gravity is regarded as a low-frequency disturbance to the system.

The equations of motion for the single-tethered system shown in Fig. 3 can be derived by exploiting the Euler–Lagrange equations [7]:

$$\mathbf{M}_1(\phi)\begin{pmatrix}\ddot{\theta}\\ \ddot{\phi}\end{pmatrix} + \mathbf{C}_1(\phi,\dot{\theta},\dot{\phi})\begin{pmatrix}\dot{\theta}\\ \dot{\phi}\end{pmatrix} + \begin{pmatrix}2m(r\cos\phi + \ell)\dot{\theta}\,\dot{\ell}\\ 2mr\cos\phi\dot{\theta}\,\dot{\ell}\end{pmatrix} = \begin{bmatrix} r+\ell\cos\phi & 1\\ r & 1\end{bmatrix}\begin{pmatrix}F\\ u\end{pmatrix} \tag{4}$$

where

$$\mathbf{M}_1(\phi) = \begin{bmatrix} I_r + m\ell^2 + 2mr\ell\cos\phi & I_r + mr\ell\cos\phi\\ I_r + mr\ell\cos\phi & I_r\end{bmatrix}$$

$$\mathbf{C}_1(\phi,\dot{\theta},\dot{\phi}) = \begin{bmatrix} -mr\ell\sin\phi\dot{\phi} & -mr\ell\sin\phi(\dot{\theta}+\dot{\phi})\\ +mr\ell\sin\phi\dot{\theta} & 0\end{bmatrix}$$

In the preceding equations, r, ℓ, and I_G denote the satellite's radius, tether length, and moment of inertia. Note that I_r is the moment of inertia about the tether attachment point A such that $I_r = I_G + mr^2$. Also, F is the force due to thruster firing, and u is the torque exerted on the c.m. by a reaction wheel assembly. It should be noted that we use the following particular definition of the $\mathbf{C}_1$ matrix [26] in Eq. (4):

$$c_{ij} = \frac{1}{2}\sum_{k=1}^{n}\frac{\partial M_{ij}}{\partial q_k}\dot{q}_k + \frac{1}{2}\sum_{k=1}^{n}\left(\frac{\partial M_{ik}}{\partial q_j} - \frac{\partial M_{jk}}{\partial q_i}\right)\dot{q}_k \tag{5}$$

This implies that $(\dot{\mathbf{M}}_1 - 2\mathbf{C}_1)$ is skew-symmetric.

C. Phase Portrait and Artificial Potential Energy

In this section, we study graphically the nonlinear trajectories of Eq. (4) by plotting a phase portrait (also commonly called a phase plane). By looking at a phase portrait, stability and trajectory information from various initial conditions $[\phi(0), \dot{\phi}(0)]$ are obtained. As shall be seen in the linearized model (Sec. II.D) as well, the nonzero rotational rate $\dot{\theta}$ adds a potential term to the dynamics, even in the absence of gravity. This artificial potential energy induced by array rotation makes the system controllable and stable. This is especially true for large classes of underactuated systems (e.g., tethered systems with $F = 0$), which are neither controllable in the absence of potential energy nor fully feedback linearizable [27].

We can multiply Eq. (4) with the fixed tether length $\dot{\ell} = 0$ by the inverse of the inertia matrix $\mathbf{M}$ to get the equation for $\ddot{\phi}$. We assume that the system rotates at a constant angular velocity ($\dot{\theta} = \omega$). Then, the homogeneous equation of ϕ results in the following second-order differential equation:

$$\frac{d}{dt}\begin{pmatrix}\phi\\ \dot{\phi}\end{pmatrix} = \begin{pmatrix}\dot{\phi}\\ -\frac{r\sin\phi}{\ell[I_G+mr^2(\sin^2\hat{\phi})]}[(I_r+mr\ell\cos\phi)(\dot{\theta}+\dot{\phi})^2+mr\ell\dot{\theta}^2\cos\phi+m\ell^2\dot{\theta}^2]\end{pmatrix} \tag{6}$$

Figure 4a shows a phase portrait of the nonlinear compound pendulum motion when the single-tethered satellite revolves around the center of the inertial frame at a constant angular speed ($\dot{\theta} = \omega$). The following physical parameters are used: $I_G = 0.0213\ \text{kgm}^2$, $m = 4.5$ kg, $r = 0.125$ m, $\omega = 0.3$ rad/s, and $\ell = 0.5$ m. It correctly predicts a pendulum libration mode. When $\dot{\phi}$ is small enough, it oscillates in a closed circle or ellipse, which is a periodic orbit of the libration motion. However, a larger $\dot{\phi}$ results in the rotation of ϕ greater than 180 deg. In reality, it will hit the tether when ϕ crosses π rad. Because ω is positive (counterclockwise) rotation, the maximum allowable value of $\dot{\phi}$, to remain in a closed orbit, is greater when $\dot{\phi}$ is positive (see Fig. 4a).

To investigate the effect of different tether lengths and angular rotation speeds, several phase plots are constructed. Figure 4b shows a phase portrait with an increased angular velocity ($\omega = 1.0$ rad/s). We can see the region of a periodic orbit has been greatly expanded. A circular orbit becomes more elliptical toward the vertical $\dot{\phi}$ axis. A similar trend is observed when we increase the tether length ℓ, in Figs. 4c and 4d.

There exist three equilibrium points in those phase portraits. Only $\phi = 0$, $\dot{\phi} = 0$ is a stable equilibrium. Along with the nominal array rotational rate ω, the equilibria of Eq. (6) define the relative [28] equilibria of the spinning tethered array. Relative equilibria are commonly found in spinning rigid bodies with symmetries. For the case of the three-dimensional free rigid body, the body is in relative equilibrium if, and only if, its angular velocity and angular momentum align, that is, if the body rotates about one of its principal axes.

D. Linearization and Pendulum Mode Frequency

Let us assume that the tether length is fixed ($\dot{\ell} = 0$) until we discuss the effect of the nonzero tether speed in Sec. II.F. We linearize Eq. (4) about the relative equilibrium point with $\dot{\theta} = \omega$, $\phi = 0$, and $\dot{\phi} = 0$, where ω denotes a nominal angular rate. Each term can be linearized as follows:

$$\begin{gathered} mrl\sin(\phi)\dot{\theta}^2 \approx mrl\omega^2\phi, \qquad mrl\sin(\phi)\dot{\phi}^2 \approx 0\\ mrl\sin(\phi)\dot{\theta}\,\dot{\phi} \approx 0, \qquad \cos\phi \approx 1\end{gathered} \tag{7}$$

The linearized equation of the motion is presented:

$$\begin{bmatrix} I_G + m(r+\ell)^2 & I_G + mr(r+\ell)\\ I_G + mr(r+\ell) & I_G + mr^2\end{bmatrix}\begin{pmatrix}\ddot{\theta}\\ \ddot{\phi}\end{pmatrix} + \begin{bmatrix}0 & 0\\ 0 & mr\ell\omega^2\end{bmatrix}\begin{pmatrix}\theta\\ \phi\end{pmatrix} = \begin{bmatrix} r+\ell & 1\\ r & 1\end{bmatrix}\begin{pmatrix}F\\ u\end{pmatrix} \tag{8}$$

It is observed that the nonzero rotational rate ω adds a potential term ($mr\ell\omega^2$) to the dynamics, even though there is no gravitational term in the model. This nonzero artificial potential energy, induced by the centripetal force associated with array rotation, plays a crucial role in making the system controllable and stable. This is especially true for underactuated tethered systems with $F = 0$, which are the focus of this paper.

A nice property about this linearized equation Eq. (8) is that we can decouple the equation for ϕ from that for θ. The first equation is merely the dynamics of a rigid body mode for θ. Because the linearized inertia matrix $\mathbf{M}_1$ in Eq. (8) is invertible, we multiply both sides of Eq. (8) by the inverse of the $\mathbf{M}_1$ matrix:

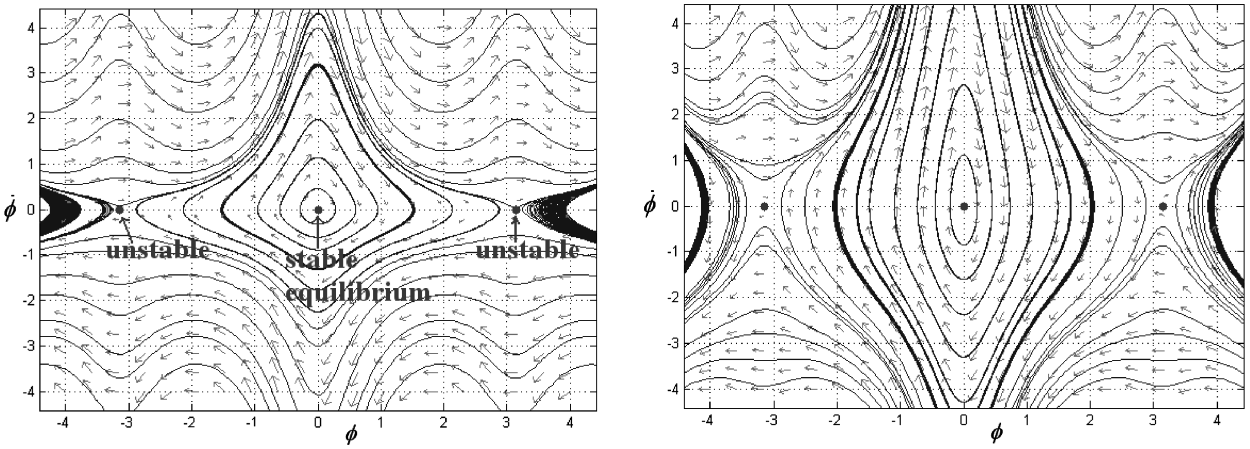

a) ω = 0.3 rad/s and ℓ = 0.5 m

b) ω=1.0 rad/s and ℓ= 0.5 m

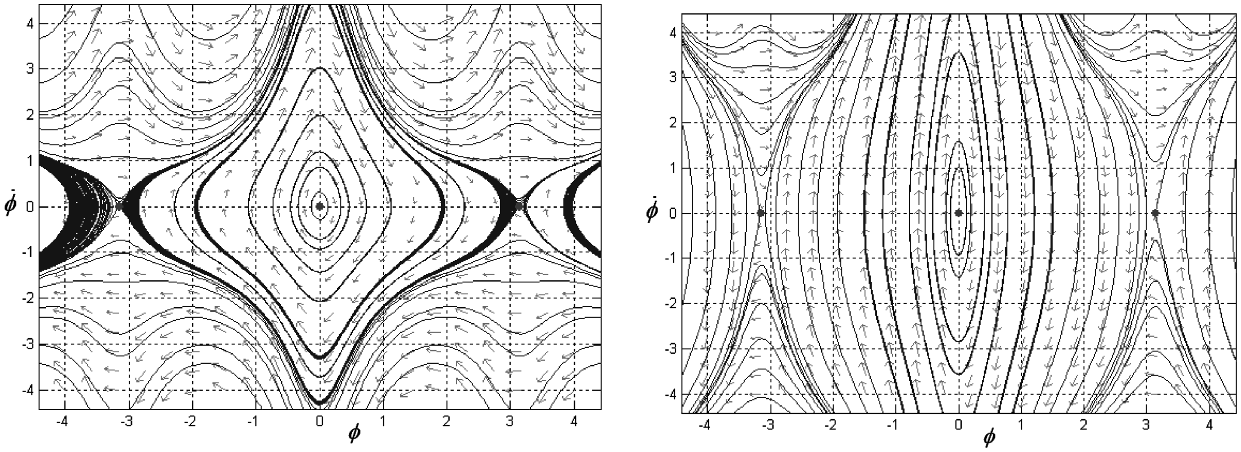

c) ω=0.3 rad/s and ℓ=2.0 m

d) ω=1.0 rad/s and ℓ=2.0m

Fig. 4 Phase portrait of Eq. (6). Dots indicate the relative equilibria. Units in rad (ϕ) and rad/s ($\dot{\phi}$).

$$\begin{pmatrix}\ddot{\theta}\\ \ddot{\phi}\end{pmatrix} + \begin{bmatrix}0 & -\frac{r\omega^2[I_G+mr(r+\ell)]}{\ell I_G}\\ 0 & \frac{r\omega^2[I_G+m(r+\ell)^2]}{\ell I_G}\end{bmatrix}\begin{pmatrix}\theta\\ \phi\end{pmatrix} = \begin{bmatrix}\frac{1}{m\ell} & -\frac{r}{I_G\ell}\\ -\frac{1}{m\ell} & \frac{r+\ell}{I_G\ell}\end{bmatrix}\begin{pmatrix}F\\ u\end{pmatrix} \tag{9}$$

The second-order nonlinear equation of motion of ϕ from the second line of Eq. (9) becomes

$$\ddot{\phi} + \omega_\phi^2\phi = -\frac{1}{m\ell}F + \frac{r+\ell}{I_G\ell}u \tag{10}$$

where ω_ϕ is the frequency of the pendular libration mode:

$$\omega_\phi = \sqrt{\frac{r[I_G + m(r+\ell)^2]}{\ell I_G}}\omega = \sqrt{\frac{r[I_r + m\ell(2r+\ell)]}{\ell I_G}}\omega \tag{11}$$

Figures 5a and 5b plot ω_ϕ as a function of ℓ and ω. Overall, the faster the array spins, the higher the pendulum mode frequency becomes. The tether length ℓ also increases the pendulum mode frequency past the minimum point (e.g., see the contour line of $\omega_\phi = 0.3$ rad/s in Fig. 5b).

E. Controllability Test

The linearized system for a single-tethered spacecraft, rotating at a constant rate $\dot{\theta} = \omega$, is derived from Eq. (9) in state-space form ($\dot{\boldsymbol{x}} = A\boldsymbol{x} + B\boldsymbol{u}$) as

$$\frac{d}{dt}\begin{pmatrix}\theta\\ \phi\\ \dot{\theta}\\ \dot{\phi}\end{pmatrix} = \begin{bmatrix}0 & 0 & 1 & 0\\ 0 & 0 & 0 & 1\\ 0 & \frac{r\omega^2[I_G+mr(r+\ell)]}{\ell I_G} & 0 & 0\\ 0 & -\frac{r\omega^2[I_G+m(r+\ell)^2]}{\ell I_G} & 0 & 0\end{bmatrix}\begin{pmatrix}\theta\\ \phi\\ \dot{\theta}\\ \dot{\phi}\end{pmatrix} + \begin{bmatrix}0 & 0\\ 0 & 0\\ \frac{1}{m\ell} & -\frac{r}{I_G\ell}\\ -\frac{1}{m\ell} & \frac{r+\ell}{I_G\ell}\end{bmatrix}\begin{pmatrix}F\\ u\end{pmatrix} \tag{12}$$

where the first matrix of the right-hand side is the 4 × 4 system matrix A and the second is the 4 × 2 input matrix B. Note that θ is easily eliminated by removing the first column and the first row of the A matrix, thereby reducing the dimension to three.

We can check if the system is really controllable around the nominal points by computing the controllability matrix:

$$\mathcal{C} = [B\ \ AB\ \ A^2B\ \ A^3B] = \begin{bmatrix}0 & 0 & \frac{1}{m\ell} & -\frac{r}{I_G\ell}\\ 0 & 0 & -\frac{1}{m\ell} & \frac{r+\ell}{I_G\ell}\\ \frac{1}{m\ell} & -\frac{r}{I_G\ell} & 0 & 0\\ -\frac{1}{m\ell} & \frac{r+\ell}{I_G\ell} & 0 & 0\end{bmatrix} \tag{13}$$

This matrix has full rank ($n = 4$). Hence, the system is fully controllable with u and F. In fact, all the states (θ, ϕ, $\dot{\theta}$, $\dot{\phi}$) are still controllable when only the torque-generating actuator u is available (e.g., RWA). The controllability matrix using the second column of the B matrix in Eq. (12) becomes

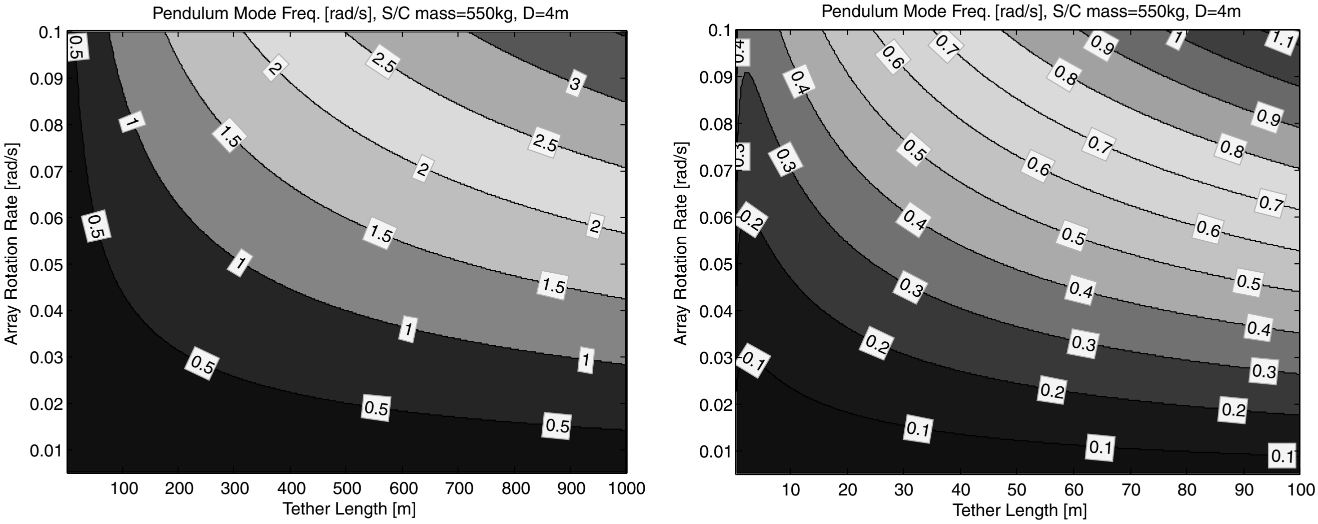

a) Natural frequency

b) Natural frequency

Fig. 5 Contour plots of the pendulum mode frequency.

$$\mathcal{C}=[B_2\ \ AB_2\ \ A^2B_2\ \ A^3B_2]$$

$$=\begin{bmatrix} 0 & -\frac{r}{I_G\ell} & 0 & \frac{r(r+\ell)\omega^2[I_G+mr(r+\ell)]}{\ell^2 I_G^2} \\ 0 & \frac{r+\ell}{I_G\ell} & 0 & -\frac{r(r+\ell)\omega^2[I_G+m(r+\ell)^2]}{l^2 I_G^2} \\ -\frac{r}{I_G\ell} & 0 & \frac{r(r+\ell)\omega^2[I_G+mr(r+\ell)]}{\ell^2 I_G^2} & 0 \\ \frac{r+l}{I_G\ell} & 0 & -\frac{r(r+\ell)\omega^2[I_G+m(r+\ell)^2]}{\ell^2 I_G^2} & 0 \end{bmatrix} \tag{14}$$

This is also a full rank ($n=4$) matrix for any nonzero ω and tether length ℓ. In addition, the tether length ℓ is directly controllable by the tether motor (see the additional controllability analysis in [7]). If a nonlinear system's linear approximations in a closed connected region U are all controllable, then, under some mild smoothness assumptions, the nonlinear system can be driven from any point in U to any point in U [26]. Its implication to the control of tethered systems is significant: the tethered satellite systems are able to spin up and resize the array without the use of propellant when operating around the relative equilibrium of a nominal array angular rate, $\dot{\theta}=\omega$. The underactuated controllers, introduced in this series, take advantage of this observation. It should be noted that the controllability matrix $\mathcal{C}$ tends to a singular matrix as the tether length ℓ tends to infinity. For example, the condition number of the controllability matrix increases as a quadratic function of the tether length. This result implies that the underactuated system using only torque input becomes less efficient in controlling the array spin rate $\dot{\theta}$ as the tether length increases, whereas control of the compound pendulum modes is effective, regardless of the tether length.

F. Effect of Varying Tether Length

In the preceding sections, the length of the tether is assumed to be invariant ($\dot{\ell}=0$). The dynamics of the varying tether length with a constant motor reel-in/out speed ($\dot{\ell}=$ constant) is investigated in this section. Similar to Sec. II.D, we linearize Eq. (4) for an array rotational rate $\dot{\theta}=\omega$, as follows:

$$\begin{pmatrix}\ddot{\theta}\\ \ddot{\phi}\end{pmatrix}+\begin{bmatrix} 2\frac{\dot{\ell}}{\ell} & 0 \\ -2\frac{\dot{\ell}}{\ell} & 0\end{bmatrix}\begin{pmatrix}\dot{\theta}\\ \dot{\phi}\end{pmatrix}+\begin{bmatrix} 0 & -\frac{r\omega^2[I_G+mr(r+\ell)]}{\ell I_G} \\ 0 & \frac{r\omega^2[I_G+m(r+\ell)^2]}{\ell I_G}\end{bmatrix}\begin{pmatrix}\theta\\ \phi\end{pmatrix}$$
$$=\begin{bmatrix} -\frac{r}{I_G\ell} \\ \frac{r+\ell}{I_G\ell}\end{bmatrix}u \tag{15}$$

where we assume that the thruster force F is not available.

Hence, the following linearized equation Eq. (12) is obtained:

$$\frac{d}{dt}\begin{pmatrix}\theta\\ \phi\\ \dot{\theta}\\ \dot{\phi}\end{pmatrix}=\begin{bmatrix} 0 & 0 & 1 & 0 \\ 0 & 0 & 0 & 1 \\ 0 & \frac{r\omega^2[I_G+mr(r+\ell)]}{\ell I_G} & -2\frac{\dot{\ell}}{\ell} & 0 \\ 0 & -\frac{r\omega^2[I_G+m(r+\ell)^2]}{\ell I_G} & 2\frac{\dot{\ell}}{\ell} & 0\end{bmatrix}\begin{pmatrix}\theta\\ \phi\\ \dot{\theta}\\ \dot{\phi}\end{pmatrix}+\begin{bmatrix} 0 \\ 0 \\ -\frac{r}{I_G\ell} \\ \frac{r+\ell}{I_G\ell}\end{bmatrix}u \tag{16}$$

Instead of showing the analytic solutions of the eigenvalues of Eq. (16) with zero F and u, a real–imaginary axis plot is presented as shown in Fig. 6. It is noted that the system is stable when the motor reels out. In other words, a positive tether speed ($\dot{\ell}>0$) results in damping of both $\dot{\theta}$ and pendulum motion of ϕ. However, we will see unstable states for a negative tether speed ($\dot{\ell}<0$). In essence, we need a stabilizing controller u for the system with the tether length decreasing. It should be noted that the deployment operation ($\dot{\ell}>0$) may also lead to system instability in the presence of orbital dynamics (gravity). For example, Kumar [9] found that the critical minimum value of spin rate in a gravity field is found to be 0.58 times the orbital rate. This indicates that the array spin rate should be fast enough to overcome the gravity effect in the deployment operation. Nonetheless, the retrieval motion is always unstable regardless of gravity.

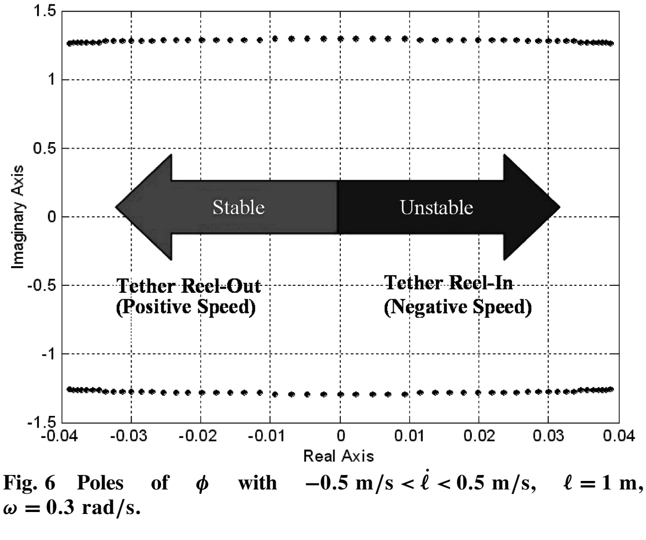

Fig. 6 Poles of ϕ with $-0.5\ \mathrm{m/s}<\dot{\ell}<0.5\ \mathrm{m/s}$, $\ell=1\ \mathrm{m}$, $\omega=0.3\ \mathrm{rad/s}$.

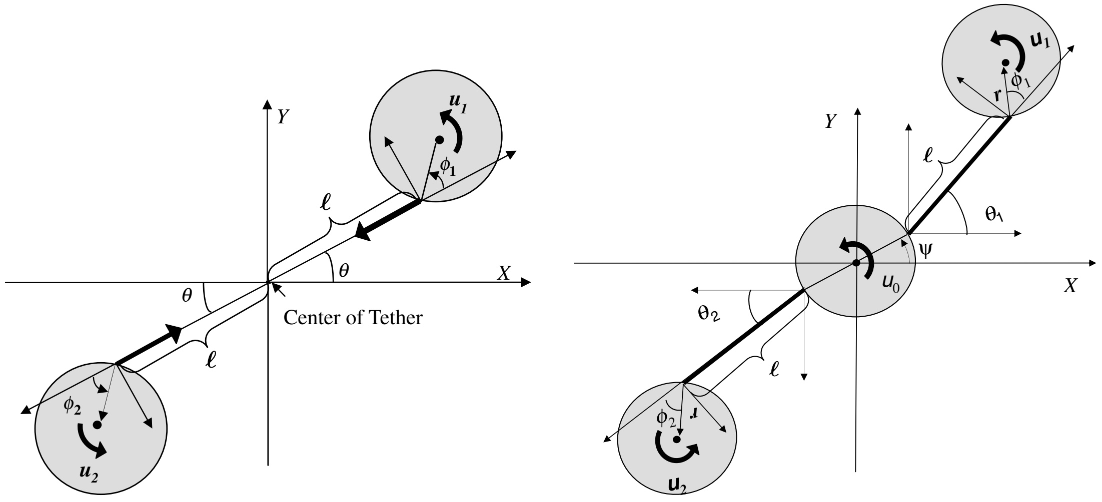

a) Two-tethered spacecraft **b) Three-tethered spacecraft**

Fig. 7 Free-body diagram of two-spacecraft and three-spacecraft systems.

The preceding linearization presents a conclusive result, which is sufficient to determine the stability of the nonlinear tethered-array dynamics. However, we can also intuitively determine the nonlinear stability by inspecting the nonlinear dynamics in Eq. (4) and invoking the Lyapunov stability theorem.

The increasing $\dot{\theta}$ with $\dot{\ell} < 0$ is easily interpreted by the conservation of angular momentum. In other words, as the size of the array decreases, the angular rate of the array rotation increases. The $\dot{\ell}\,\dot{\theta}$ term in Eq. (4) can be interpreted as the Coriolis torque in a rotating object, which exerts a force sideways, thereby exciting the pendulum mode $(\phi, \dot{\phi})$ and making the system unstable. Hence, $\dot{\ell} < 0$ adds negative damping, driving the system to be unstable. This can be proven by the instability theorem [26] (see [7] for the proof).

G. Multivehicle Dynamics

The dynamics of two tethered satellites in the plane of rotation, shown in Fig. 7a, are derived in [8]:

$$\mathbf{M}_2(\phi_1,\phi_2)\begin{pmatrix}\ddot{\theta}\\ \ddot{\phi}_1\\ \ddot{\phi}_2\end{pmatrix} + \mathbf{C}_2(\phi_1,\phi_2,\dot{\theta},\dot{\phi}_1,\dot{\phi}_2)\begin{pmatrix}\dot{\theta}\\ \dot{\phi}_1\\ \dot{\phi}_2\end{pmatrix} + \begin{pmatrix}2m(r\cos\phi_1 + r\cos\phi_2 + 2\ell)\dot{\theta}\,\dot{\ell}\\ 2mr\cos\phi_1\dot{\theta}\,\dot{\ell}\\ 2mr\cos\phi_2\dot{\theta}\,\dot{\ell}\end{pmatrix} = \begin{pmatrix}u_1+u_2\\ u_1\\ u_2\end{pmatrix} \tag{17}$$

where $\mathbf{M}_2(\phi_1,\phi_2)$ and $\mathbf{C}_2(\phi_1,\phi_2,\dot{\theta},\dot{\phi}_1,\dot{\phi}_2)$, given in [8], can also be derived by the parallel combination of the two independent single-tethered dynamics. Note that $\dot{\mathbf{M}}_2 - \mathbf{C}_2$ is skew-symmetric.

Because ℓ is defined as the length of the tether from the origin to the spacecraft attachment point, the total tether length is now 2ℓ and $\dot{\ell}$ is half the rate of change of the total tether length. The array angular rate $\dot{\theta}$ is assumed to be the same for both satellites. This is especially true when the tether is in tension. Furthermore, the mass and inertia properties are assumed to be roughly the same. These geometric symmetry properties are pervasive in stellar interferometers where subtelescopes must be identical for interferometric beam combining. Note that both the single and two-spacecraft systems are symmetric in mechanics [28] with respect to θ, thereby resulting in an inertia matrix that is independent of θ.

1. Linearization and Controllability Analysis

We can also linearize the two-body dynamics with the fixed tether length ($\dot{\ell} = 0$) in Eq. (17) with respect to the relative equilibrium, $\dot{\theta} = \omega$, $\phi_1 = 0$, $\dot{\phi}_1 = 0$, $\phi_2 = 0$, and $\dot{\phi}_2 = 0$:

$$\begin{pmatrix}\dot{\theta}\\ \dot{\phi}_1\\ \dot{\phi}_2\\ \ddot{\theta}\\ \ddot{\phi}_1\\ \ddot{\phi}_2\end{pmatrix} = \begin{bmatrix}0 & 0 & 0 & 1 & 0 & 0\\ 0 & 0 & 0 & 0 & 1 & 0\\ 0 & 0 & 0 & 0 & 0 & 1\\ 0 & \frac{r(I_r+mr\ell)\omega^2}{2I_G\ell} & \frac{r(I_r+mr\ell)\omega^2}{2I_G\ell} & 0 & 0 & 0\\ 0 & -\frac{r[(I_r+mr\ell)^2+2I_Gm\ell^2]\omega^2}{2I_GI_r\ell} & -\frac{r(I_r+mr\ell)^2\omega^2}{2I_GI_r\ell} & 0 & 0 & 0\\ 0 & -\frac{r(I_r+mr\ell)^2\omega^2}{2I_GI_r\ell} & -\frac{r[(I_r+mr\ell)^2+2I_Gm\ell^2]\omega^2}{2I_GI_r\ell} & 0 & 0 & 0\end{bmatrix} \times \begin{pmatrix}\theta\\ \phi_1\\ \phi_2\\ \dot{\theta}\\ \dot{\phi}_1\\ \dot{\phi}_2\end{pmatrix} + \begin{bmatrix}0 & 0\\ 0 & 0\\ 0 & 0\\ -\frac{r}{2I_G\ell} & -\frac{r}{2I_G\ell}\\ \frac{1}{2}(\frac{r+\ell}{I_G\ell}+\frac{1}{I_r}) & \frac{r(I_r+mr\ell)}{2I_G\ell I_r}\\ \frac{r(I_r+mr\ell)}{2I_G\ell I_r} & \frac{1}{2}(\frac{r+\ell}{I_G\ell}+\frac{1}{I_r})\end{bmatrix}\begin{pmatrix}u_1\\ u_2\end{pmatrix} \tag{18}$$

where only torque actuation (u_1, u_2) is available.

It can also be shown that the controllability matrix with any nonzero ω yields a full rank of six, justifying the underactuated control approach that uses only reaction wheels. This result can also be extended to the case of nonzero $\dot{\ell}$.

2. Three-Inline Configuration

The equations of motion for a three-spacecraft inline configuration shown in Fig. 7 are also given in [8]. The definition of the generalized coordinates, θ_1 and θ_2, largely affects the complexity of the dynamic equations [7]. Similar to the previous section, the corresponding nonlinear system can be linearized about a nominal rotational rate, $\dot{\psi}$, $\dot{\theta}_1$, $\dot{\theta}_2 \approx \omega$, whereas other relative angles and their rates are sufficiently close to zero such that $\theta_1 - \psi$, $\theta_2 - \psi \approx 0$, and ϕ_1, $\dot{\phi}_1$, ϕ_2, $\dot{\phi}_2 \approx 0$:

$$[\mathbf{M}]\ddot{\mathbf{q}} + [\mathbf{K}]\mathbf{q} = (\tau) \tag{19}$$

where

$$[\mathbf{M}] = \begin{bmatrix} I_G + 2mr^2 & mr(\ell + r) & mr^2 & mr(\ell + r) & mr^2 \\ mr(\ell + r) & I_G + m(\ell + r)^2 & I_G + mr(\ell + r) & 0 & 0 \\ mr^2 & I_G + mr(\ell + r) & I_G + mr^2 & 0 & 0 \\ mr(\ell + r) & 0 & 0 & I_G + m(\ell + r)^2 & I_G + mr(\ell + r) \\ mr^2 & 0 & 0 & I_G + mr(\ell + r) & I_G + mr^2 \end{bmatrix}$$

$$[\mathbf{K}] = \begin{bmatrix} 2mr(\ell + r)\omega^2 & -mr(\ell + r)\omega^2 & -mr^2\omega^2 & -mr(\ell + r)\omega^2 & -mr^2\omega^2 \\ -mr(\ell + r)\omega^2 & mr(\ell + r)\omega^2 & mr^2\omega^2 & 0 & 0 \\ -mr^2\omega^2 & mr^2\omega^2 & mr(\ell + r)\omega^2 & 0 & 0 \\ -mr(\ell + r)\omega^2 & 0 & 0 & mr(\ell + r)\omega^2 & mr^2\omega^2 \\ -mr^2\omega^2 & 0 & 0 & mr^2\omega^2 & mr(\ell + r)\omega^2 \end{bmatrix}$$

$$(\tau) = \begin{pmatrix} u_0 \\ (r + \ell)F_1 + u_1 \\ rF_1 + u_1 \\ (r + \ell)F_2 + u_2 \\ rF_2 + u_2 \end{pmatrix}, \quad \text{and} \quad \mathbf{q} = \begin{pmatrix} \psi \\ \theta_1 \\ \phi_1 \\ \theta_2 \\ \phi_2 \end{pmatrix}$$

It is straightforward to show that the three-spacecraft inline system is fully controllable by a reaction wheel in each spacecraft (u_0, u_1, and u_2 in Fig. 7b). Moreover, a stability analysis, similar to Sec. II, results in the same conclusion that the spinning tethered system goes unstable while retracting the tether. Without loss of generality, this result can be extended to a three-spacecraft triangular configuration (see [7]).

III. Linear Control Design

Motivated by the controllability analysis introduced in the previous section, we present a gain-scheduling linear control technique that controls all the relevant degrees of freedom without using linear thruster forces. We first introduce the control law for the linearized time-varying dynamic model of the single-spacecraft tethered system shown in Fig. 3. Then, we show that such a decentralized control law, designed from the singled-tethered system, ensures the stability of a multispacecraft system, thereby eliminating the need for any intersatellite communication.

A. Gain-Scheduled Linear Quadratic Regulator Approach

Even though we embraced this linear control technique in the actual implementation in Sec. V, for simplicity, we emphasize that the linearization-based control would only provide a local stability result, as opposed to global convergence of the nonlinear control strategies introduced in the second paper [29] of this series. Again, the controllability analysis in Section II states that the spinning underactuated tethered system is fully controllable around the relative equilibrium manifold ($\dot{\theta} = \omega$, $\phi = 0$, and $\dot{\phi} = 0$). This indicates that the configuration variable ϕ is not subject to a large angle rotation, as seen in a swing-up maneuver of the acrobot, but rather has to be stabilized at the equilibrium $\phi = 0, \dot{\phi} = 0$ at all times. Thanks to this requirement, we can expect that the linear LQR control can perform reasonably well around the equilibrium point.

Recalling that the linearized equations in Eq. (12) are fully controllable using only the torque input u, we can construct a linear feedback control law $u = K(\phi, \dot{\theta}, \dot{\phi})$, based upon the following linearized equations of motion:

$$\frac{d}{dt}\begin{pmatrix} \phi \\ \dot{\theta} \\ \dot{\phi} \end{pmatrix} = \begin{bmatrix} 0 & 0 & 1 \\ \frac{r\omega^2(I_r + m\ell)}{\ell I_G} & 0 & 0 \\ -\frac{r\omega^2[I_r + m\ell(2r + \ell)]}{\ell I_G} & 0 & 0 \end{bmatrix}\begin{pmatrix} \phi \\ \dot{\theta} \\ \dot{\phi} \end{pmatrix} + \begin{pmatrix} 0 \\ -\frac{r}{I_G \ell} \\ \frac{r + \ell}{I_G \ell} \end{pmatrix} u \tag{20}$$

where we intentionally left out the state θ because it is merely a rigid body rotation mode.

We assume that all the states ($\phi, \dot{\theta}, \dot{\phi}$) are available by the Kalman filter, which is presented in Sec. IV.C. Then, we can design an LQR controller, which specifically addresses the issue of achieving a balance between good system response and minimizing the control effort required. The LQR control also possesses very good stability margins.

Because the A matrix in Eq. (20) is a function of $\dot{\theta}$ and the tether length ℓ, the optimal LQR gains are computed for a range of angular rates and tether lengths. A continuous function is then fit to these discrete gains. Then, the gain-scheduled LQR gain is a continuous function of $\dot{\theta}$ and tether length ℓ as depicted in Fig. 8:

$$u = -K_1(\dot{\theta}, \ell)\phi - K_2(\dot{\theta} - \dot{\theta}_d) - K_3(\dot{\theta}, \ell)\dot{\phi} \tag{21}$$

where K_2 turns out to be independent of $\dot{\theta}$ and ℓ.

Such a gain-scheduled LQR controller has been successfully implemented in the SPHERES test bed, as shall be seen in Sec. V. This gain-scheduling approach has been a popular subject of research as alternative form of nonlinear control, as indicated in a recent survey paper [30]. One merit of the linearization is that it permits the use of mature and well-established linear control techniques to address nonlinear problems. However, stability can be assured only locally and in a "slow-variation" setting [30]. To ensure global or semiglobal stability results, we have to use nonlinear underactuated control methods, as discussed in [7].

B. Stability of Decentralized Control

It is shown in [8] that a linear decentralized control law in Eq. (21)

$$\begin{aligned} u_1 &= -K_1\phi_1 - K_2(\dot{\theta} - \dot{\theta}_d) - K_3\dot{\phi}_1 \\ u_2 &= -K_1\phi_2 - K_2(\dot{\theta} - \dot{\theta}_d) - K_3\dot{\phi}_2 \end{aligned} \tag{22}$$

stabilizes the linearized tethered two-spacecraft dynamics of Eq. (17) if $rK_2 < (r + \ell)K_3$, $K_1 > 0$, $K_2 > 0$. Furthermore, it is proven that such a decentralized control synchronizes the compound pendulum oscillation, ϕ_1 and ϕ_2. This result can be extended to arbitrary large circular arrays of spacecraft as well as three-spacecraft inline configuration, as proven in [8]. Consequently, we can stabilize a coupled tethered array without the need for any intersatellite communication, thereby reducing the complexity in both the hardware and software. We can also expect that the decentralized control techniques introduced in this section possess the same stability property for a multivehicle underactuated system if the behavior of the closed-loop systems is sufficiently close to the

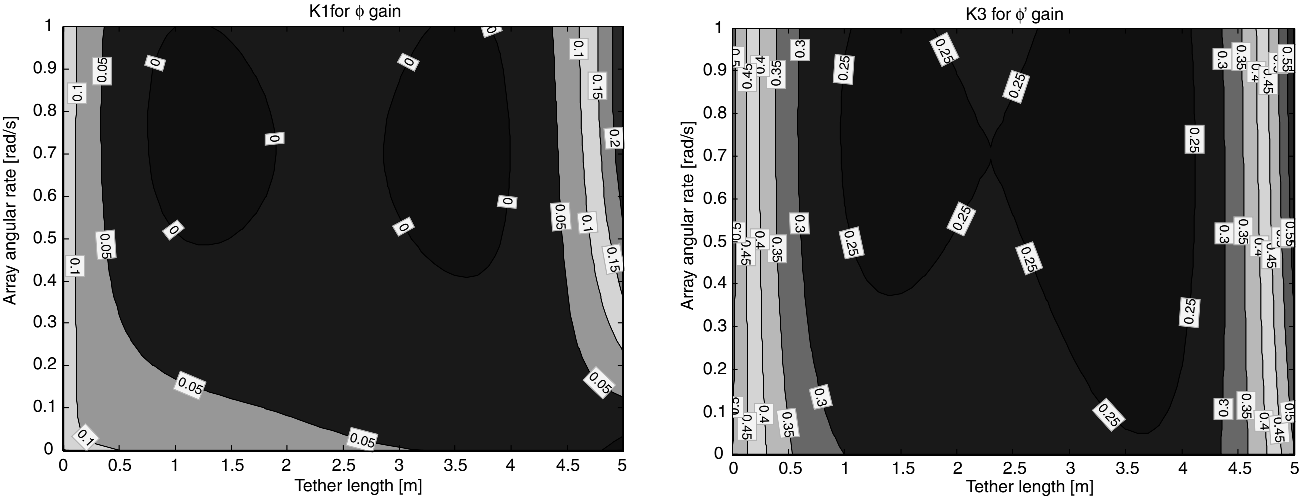

a) K1 for ϕ

b) K3 for $\dot{\phi}$

Fig. 8 LQR gains scheduled for a range of $\dot{\theta}$ and ℓ.

linearized dynamics. In the case of spinning tethered arrays, this is particularly true for a regulatory control in which a desired trajectory is time-invariant. Note that the stability proof of decentralized nonlinear control for underactuated tethered spacecraft is more involved [7].

IV. Experimental Validation using SPHERES

We describe the experimental setup in this section, whereas experimental results are summarized in Sec. V. The aim of the control experiments introduced in this paper can be stated as follows. First, we experimentally demonstrate the effectiveness of the decentralized underactuated control framework that does not use thrusters for spinning tethered formation flying arrays. Second, we investigate the feasibility and practicality of the proposed decentralized and relative estimator using force-torque sensors and rate gyroscopes.

A. Overview of SPHERES Satellite

The MIT Space Systems Laboratory (MIT-SSL) developed the multiple nanosatellite test bed called SPHERES to advance

a) Formation flying experiments on ISS

b) Formation flying experiments onboard KC-135 flight

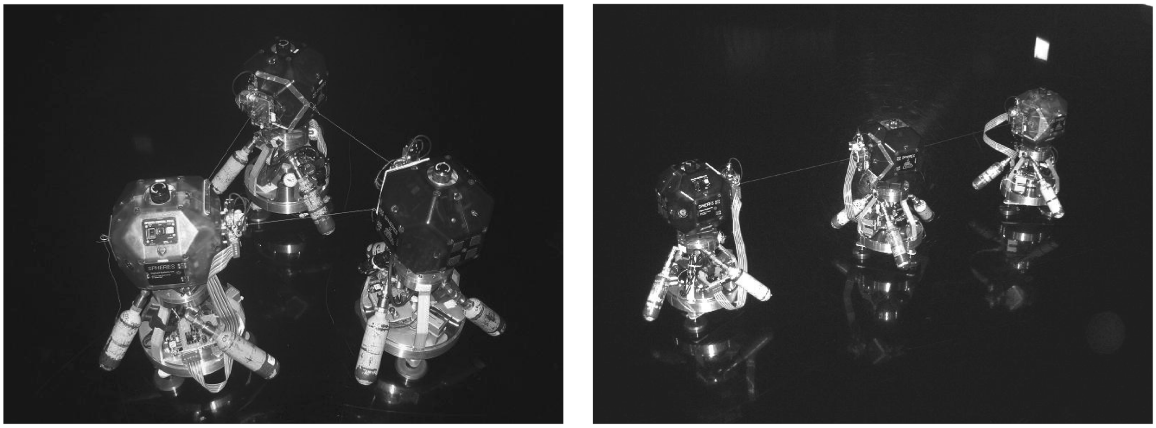

c) Three triangular configuration on NASA MSFC flat floor

d) Three inline configuration on NASA MSFC flat floor

Fig. 9 Three operational environments of SPHERES: a) ISS, b) KC-135 reduced-gravity flight, c–d) NASA MSFC flat floor.

Table 1 SPHERES properties

Properties	SPHERES satellite	With RWA air-carriage
Diameter	0.25 m	0.25 m
Mass	3.87 kg	15.856 kg
Number of CO_2 tanks	1	4
Mass with full tanks	4.5 kg	20.346 kg
Moment of inertia	$0.0213\ \mathrm{kg \cdot m^2}$	$0.178\ \mathrm{kg \cdot m^2}$
Max linear force actuation	0.24 N	0.24 N
Max torque actuation	0.012 Nm (thrusters)	0.207 Nm (RWA)
Power	15 W	30 W
Battery life	1.5 h	1.5 h

metrology, control, and autonomy technologies for use in formation flight and autonomous docking, rendezvous, and reconfiguration algorithms (see Fig. 9). To support tethered formation flying experiments with the SPHERES test bed, a new suite of hardware has been designed and added. The aim of the present section is to describe such recent improvements to the SPHERES, including a new tether reel mechanism, a force-torque sensor to measure bearing angle, and an air-bearing carriage with a reaction wheel.

At the time of writing, several SPHERES nanosatellites were launched to the International Space Station (ISS) for control experiments in a three-dimensional environment. Motivated by the successful experimental results in this paper, tethered formation flying experiments on ISS are currently being pursued. The microgravity facility in ISS provides six degrees of freedom for each satellite to fully test control and estimation algorithms for NASA's future stellar interferometer missions, such as SPECS [3]. Meanwhile, we verify the proposed control algorithms in the two-dimensional flat floor facilities at MIT and NASA Marshall Space Flight Center (MSFC). The three main operational environments of the SPHERES test bed are presented in Fig. 9. The top two pictures show the zero-gravity 6 DOF environment on ISS (top left) and NASA's KC-135 reduced-gravity aircraft (top right). The bottom pictures depict SPHERES sitting on the air-bearing carriages at the NASA MSFC flat floor, which provides 3 DOF: yaw rotation and x, y translations.

The individual self-contained satellites have the ability to maneuver in up to 6 DOF (three rotations and three translations), to communicate with each other and with the laptop control station, and to identify their position and attitude with respect to each other and to the experiment global reference frame. The physical characteristics of a SPHERES satellite are summarized in Table 1. The original SPHERES metrology system, using the ultrasound time-of-flight and rate gyroscopes, provides metrology information to the satellites in real-time. Because no global metrology system like GPS is actually available in deep-space missions, the tethered-SPHERES system uses a relative metrology system using the four ultrasound receivers (24 in total per each SPHERES satellite) on the line-of-sight face and the onboard beacon of the adjacent SPHERES satellite (see Fig. 10). The relative metrology system is a pseudo-GPS ranging system that uses ultrasonic time-of-flight measurements from the target onboard beacon to the ultrasound (U/S) microphones distributed on the surface of each satellite. These time-of-flight measurements are converted to ranges and are then used to derive relative attitude and rate $(\phi, \dot{\phi})$ with respect to the reference frame using a series of extended Kalman filters (EKF). An additional Kalman filter, incorporating the gyroscope measurement, estimates all the states (compound pendulum mode and array rotation rate) needed for each satellite. A flow of measurement data is illustrated in Fig. 10. Each estimation algorithm is decentralized in the sense that it uses the single-tethered dynamics in Eq. (4).

Each SPHERES satellite comes with an expansion port that provides a connectivity to the auxiliary hardware (see Fig. 10). A tether deployment and retraction mechanism with tether force-torque sensors has been added to this expansion port to support the tethered formation tests, which is detailed in the subsequent sections.

B. Flight Quality Tether Reel with Force-Torque Sensor

The SPHERES satellite, with a prototype version of the tether reel with a force-torque sensor, is mounted on an air-bearing carriage equipped with a reaction wheel in Fig. 10. Because of the increased overall weight of the system, we converted a single-puck system back to a three-puck system. The air-bearing carriages require three CO_2 tanks, which allow for continuous operations of up to 30 min. The tether-reel mechanism attaches to the SPHERES satellite via the expansion port, allowing for data and power transmission from the satellite. The prototype tether reel includes a motor and spool assembly to reel the tether in and out, as well as a force/torque sensor

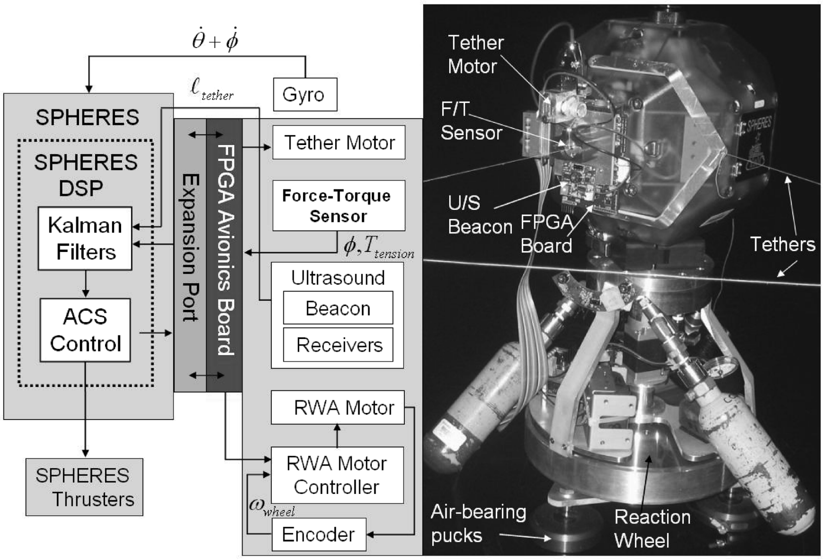

Fig. 10 SPHERES satellite on the new air-bearing carriage with a reaction wheel and its block diagram of signal and data transfer.

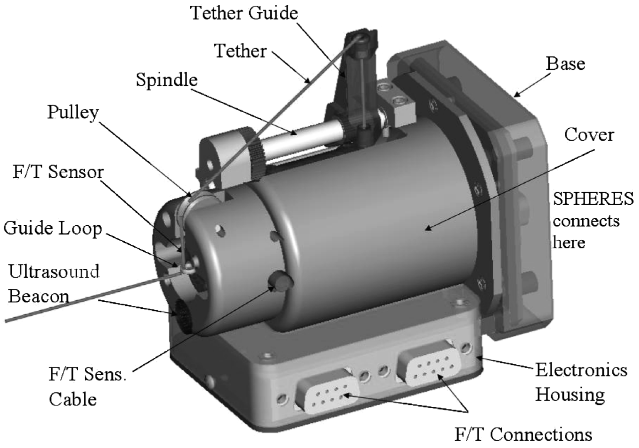

Fig. 11 Space flight version of tether-reel mechanism (courtesy of Payload Systems, Inc.)

and ultrasound sensor to measure relative position and bearing of the neighboring satellite. A new flight tether reel is being developed for experiments in the ISS.

Figure 11 is a CAD rendering of the new ISS-flight tether reel developed by the MIT-SSL and Payload Systems, Inc. The new version is designed to hold 10 m of tether. Some of the key design advantages of the new tether reel include an arm that moves along a shaft to ensure that the tether is evenly applied to the spool, as it reels in, and to prevent loss of tension. The spindle and tether guide maintain tension in the tether at all times. Rubber grommets provide friction so the tether has to be pulled onto the spool and pulled off of the spool. The spindle is threaded to move the guide approximately one tether width per revolution of the spool.

Three different kinds of electronic sensor systems are embedded in the tether-reel mechanism. First, a 6 DOF F/T sensor measures tether tension and bearing angles. Second, the ultrasound beacon emits an ultrasonic signal to adjacent SPHERES for range and relative attitude measurements. Third, the new flight version of the tether reel will be equipped with a tether motor encoder to directly measure the tether length. Such a motor encoder is not present in the prototype version shown in Fig. 10.

The previous generation of the tethered-SPHERES system could not measure tensile forces of the tether or slackness. One possible solution is to implement a strain gauge as in the case of another tethered-spacecraft test bed [23]. One big drawback of such a system is that it only allows for force measurements in one direction. Consequently, a 6 DOF F/T sensor (commonly called a load cell) is selected for the SPHERES system. The selected load cell, ATI Nano-17, can measure forces and torques in all three dimensions, and its compact size (diameter = 0.669 in. and height = 0.571 in.) allows it to fit into the small tether reel. It has a range up to 17 N for the z direction along the tether and 12 N for the x and y directions. The resolution is 1/160 N.

An F/T sensor will be used to measure the bearing angle ϕ that the tether makes with respect to the satellite in the horizontal plane. The new F/T sensor-based system simply compares two force outputs (F_x and F_y) to calculate the bearing angle ϕ (see Fig. 12). The details of the metrology system are expanded in Sec. IV.C.

C. New Relative Sensing and Decentralized Estimator

Any state feedback control algorithm requires that all states be strictly available for feedback. The role of the decentralized and relative estimator is to provide state estimates (tether length, and all the states including the bearing angle ϕ) independently of the satellites. The decentralized estimation, along with the decentralized controller, enables simple independent control of each satellite without the need for intersatellite communications. This will significantly simplify both the control algorithm and hardware implementation. The decentralized scheme is realized by the decoupling technique discussed in [8].

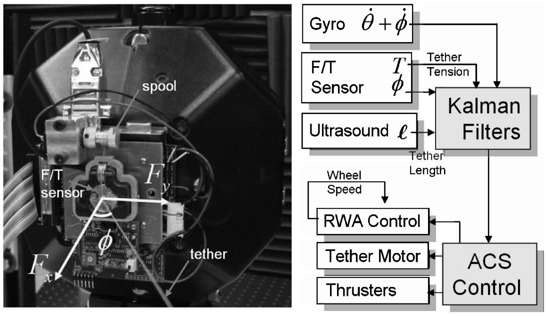

Fig. 12 New bearing angle ϕ metrology system using a force-torque sensor (ϕ in the negative direction).

In previous experiments using SPHERES [8], we relied on the SPHERES built-in ultrasound metrology system (see [7] for the description on the U/S-based method). There are several reasons why we needed to develop a new sensing mechanism. First, the best practical resolution that the current U/S system can achieve is 1 cm. This results in merely a few degrees of resolution in bearing angle for a 20 cm tether length. Second, the U/S system does not work well in close proximity due to the cone angle (±30 deg) of U/S beacon. Experiments also reveal that measurements within 15 cm tend to be inaccurate. Last, the U/S system has a limitation in bandwidth (10 Hz).

The new bearing angle measurement system using a force-torque sensor was devised to resolve all of the aforementioned identified issues. A brief description of its estimator design is presented.

As shown in Fig. 12, the tether coming from the motor spool is bent 90 deg on the horizontal plane, and goes toward the other adjacent SPHERES. Forces are exerted on the F/T sensor through a frictionless ring.

To show that this setup can also measure the out-of-plane angle ϕ_z in Fig. 13a, a general three-dimensional case is considered first. From the free-body diagram of this setup (Fig. 13), we can determine the tension and bearing angles. Then, we can solve for T, ϕ (planar pendulum mode angle), and ϕ_z (vertical angle):

$$T = \frac{F_x^2 + F_y^2 + F_z^2}{2F_z}, \qquad \phi = \tan^{-1}\frac{F_y}{F_x}$$
$$\phi_z = \sin^{-1}\frac{F_z^2 - F_x^2 - F_y^2}{F_x^2 + F_y^2 + F_z^2} \tag{23}$$

where T is the tether tension, which remains the same at all locations in the tether for the case of inextensible and massless tethers. Also, F_x, F_y, and F_z denote force measurements of the F/T sensor in the x, y, and z directions, respectively.

For the experiments on the flat floor facility, presented in this paper, only planar motions characterized by ϕ are considered, as illustrated in Figs. 12 and 13b. We use the relationship

$$\phi = \tan^{-1}\frac{F_y}{F_x} = \sin^{-1}\frac{F_y}{F_x^2 + F_y^2} \tag{24}$$

and the sensitivity matrix given by the manufacturer to compute ϕ from raw six channel F/T sensor outputs. Then, the ϕ measurement is incorporated in the Kalman filter to distinguish $\dot{\phi}$ from the combined

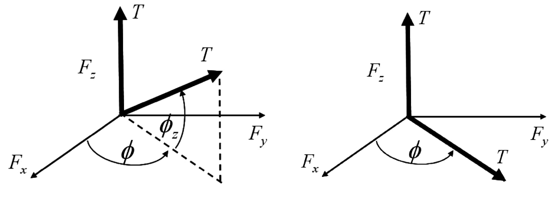

a) 3-D setup **b) 2-D setup**

Fig. 13 Forces on the F/T sensor of the tether reel, where the z axis indicates the vertical direction to the tether spool in Fig. 12.

angular rate ($\dot{\theta} + \dot{\phi}$) measured by the gyroscope. The measurement equation incorporating both the gyro measurement and the ϕ angle measurement from the F/T sensor, results in

$$y = \begin{bmatrix} \text{gyro measurement} \\ \phi \,\text{from F/T sensor} \end{bmatrix} = C\mathbf{x} + v = \begin{bmatrix} 0 & 1 & 1 \\ 1 & 0 & 0 \end{bmatrix} \begin{pmatrix} \phi \\ \dot{\theta} \\ \dot{\phi} \end{pmatrix} + v \tag{25}$$

which makes the system fully observable. The algorithm formulation of the implemented Kalman filter can be found in [7].

V. Results of Closed-Loop Experiments

The proposed approach to reduce the complexity of controlling multiple spacecraft connected by tethers is decentralization by oscillation synchronization of the compound pendulum modes [8]. We successfully performed all of the underactuated control tests using this decentralization technique. In this manner, we were able to dramatically increase the control bandwidth and reliability by eliminating the need for intersatellite communications. We present key closed-loop control results.

A. Decentralized Gain-Scheduled LQR Control

Figures 14 and 15 show the experimental data of a spin-up and deployment maneuver on the NASA MSFC flat floor, using two tethered SPHERES controlled using decentralized control laws. Still pictures from the video of the same test are presented in Fig. 16. Such a maneuver emulates a possible mission scenario in which a completely docked, tethered-spacecraft array is deployed from a mother spacecraft. All the data were transmitted to the laptop computer at the frequency of 10 Hz in real-time via the wireless RF communication. It should also be noted that all the state estimates are delivered from the Kalman filter, which incorporates both the F/T sensor measurements and the angular rates from the gyroscope, as described in Sec. IV.C.

The controller implemented in this test was a decentralized gain-scheduled LQR controller running at 100 Hz. The scheduled LQR gain is a continuous function of $\dot{\theta}$ but a discrete function of ℓ. This controller is significant in its own right, because it validates the feasibility of the minimal fuel control approach by controlling all the relevant degrees of freedom, including the array spin rate, using only the reaction wheels.

The top plot of Figs. 14 and 15 shows the actual array angular rate $\dot{\theta}$ as it is commanded to follow a desired trajectory $\dot{\theta}_{\text{ref}}$. For SPHERE #1, the rms of the error between $\dot{\theta}$ and $\dot{\theta}_{\text{ref}}$ after the initial spin-up ($t \geq 44.8$ s) is $0.04\ \text{rad/s}$, ignoring the transient period

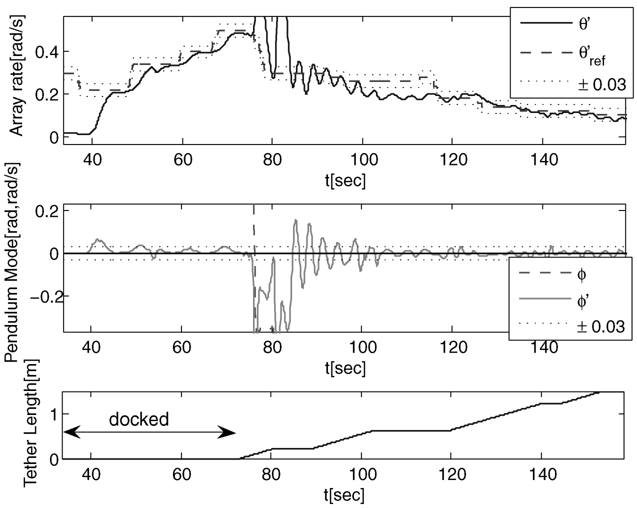

Fig. 14 State estimates and commands from SPHERE #1 during spin-up and deployment of the two-satellite tethered formation using gain-scheduled LQR.

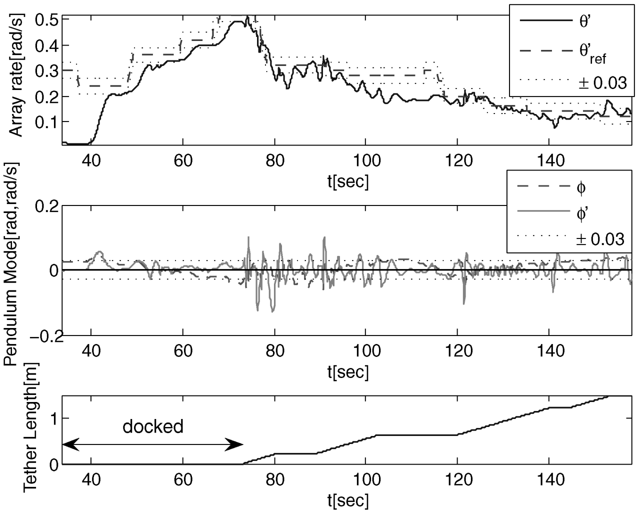

Fig. 15 State estimates and commands from SPHERE #2 during spin-up and deployment of the two-satellite tethered formation using gain-scheduled LQR.

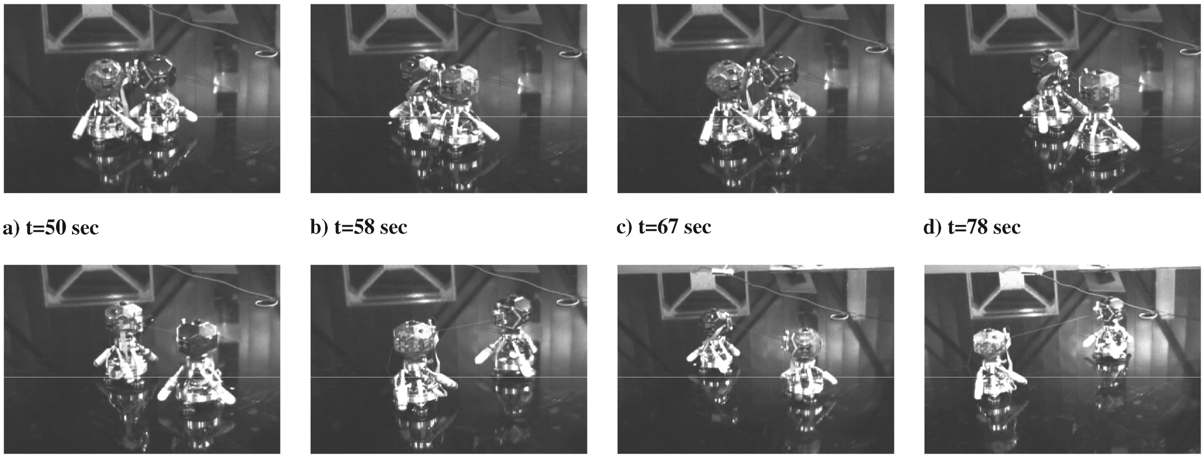
a) t=50 sec
b) t=58 sec
c) t=67 sec
d) t=78 sec
e) t=85 sec
f) t=95 sec
g) t=110 sec
h) t=130 sec

Fig. 16 Two SPHERES spin-up maneuver.

($t = 75$–86 s), which occurred due to the abrupt movement of the tether motor at 75 s. Such an undesirable response arises due to two problems: the initial stiction of the tether motor and the occasional tangling of the tether on the motor spool. These issues will be resolved in the new flight version described in Sec. IV.B. Nevertheless, the tracking error remained effectively well within ± 0.03 rad/s (1.7 deg/s) at the steady state. During the period of $t = 100$–112 s, both the satellites were spinning on a particularly rough portion of the floor, thereby degrading the tracking performance.

While tracking the desired trajectory, the controller minimizes the compound pendulum motions $(\phi, \dot{\phi})$, shown in the middle plot of each figure. The ϕ and $\dot{\phi}$ before 75 s should be discarded because the two SPHERES were docked, thereby preventing compound pendulum motion. The estimated tether length ℓ in the bottom plot indicates that the two SPHERES were completely docked when they started from rest ($\dot{\theta} = 0$) at 34 s. The estimated tether length was computed offline from the on/off time history of the tether motor, because range measurements from the U/S system were not available in real-time due to the blocked infrared (IR) transmission.

The rms errors of the compound pendulum mode, ignoring the rough period ($t = 75$–86 s) are found to be smaller than 0.03 rad/s (1.7 deg/s). In particular, the bearing angle $\dot{\phi}$ for SPHERE #1 remained within ± 0.03 rad/s (1.7 deg/s) for 91% of the time span, whereas the ϕ measurement failed for some unknown reason. The particular LQR controller implemented in this test had a zero ϕ gain, thereby minimizing the effect of such a sensor failure. For SPHERE #2, ϕ remained within the bound of ± 0.03 rad for 90% of time, whereas $\dot{\phi}$ remained within ± 0.03 rad/s for 91.3% of time. The experimental results of the decentralized LQR control are further analyzed in the next section.

B. Further Analyses and Comparison with Previous Results

Even though the preceding results show the controller effectively tracking a desired trajectory under various conditions, the harsh surface friction, and its irregularity depending on location, makes it difficult to identify the sources that degrade the control performance. As a result, the following control experimental results collected from the MIT glass table are presented for further analysis.

Figure 17 describes a single-SPHERE control experiment using the gain-scheduled LQR controller. The test starts with the SPHERE freely rotating around a stationary post (see Fig. 3b). The control torque is turned on at $t = 85$ s. The figure shows a successful regulation of the angular rate $\dot{\theta}$ to the target rate of 0.3 rad/s, while minimizing the compound pendulum mode, ϕ and $\dot{\phi}$. More specifically, the rms errors of ϕ and $\dot{\phi}$ at the steady state ($t = 100$–180 s) are 0.0175 rad and 0.009 rad/s, respectively. We can also state that the $\dot{\phi}$ error remained within ± 0.015 rad/s for 91% of the time, which resulted in more than 25 dB of attenuation of the compound pendulum oscillation. The tracking error between the target angular rate 0.3 rad/s and $\dot{\theta}$ has an rms error of 0.0055 rad/s. In essence, the performance of the LQR control on the glass table is much more efficient compared with the results obtained at the NASA MSFC flat floor shown in Figs. 14 and 15. We can attribute this difference to the higher surface friction of the NASA MSFC flat floor.

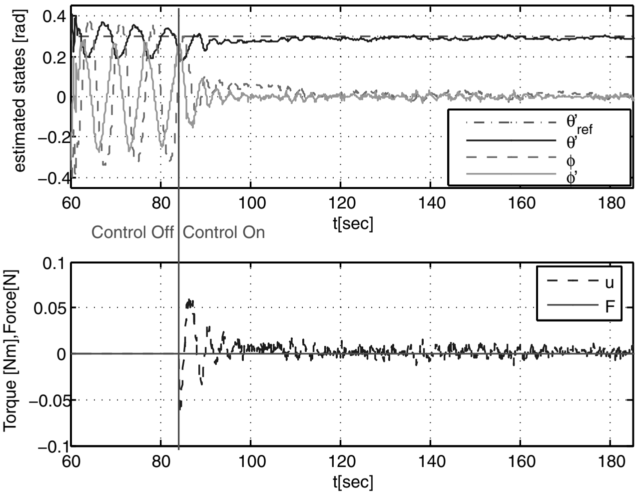

Fig. 17 Gain-Scheduled LQR control on the MIT glass table.

VI. Conclusions

The SPECS mission will use tethered formation flight to achieve its large baseline requirement. This paper has studied the potential of a new actuation method which uses only reaction wheels for in-plane (aperture pupil plane) rotation. This work is motivated by the controllability analysis, indicating that the array spin rate and relative attitude are controllable by using only torque input. Although the effectiveness of such an underactuated strategy decreases with increasing array size, the proposed method would significantly save the mass required for fuel to control the rotation rate of the tethered array in a more compact configuration.

We have emphasized that the stability and controllability analysis is based on the modeling in the two-dimensional plane. The rationale behind the reduced dynamics modeling is that the symmetry of a spinning array can be exploited to decouple the rotational in-plane motions (aperture pupil plane) from the out-of-plane motions. In addition, the dynamics modeling in this paper has facilitated nonlinear spatial decoupling of multiple-spacecraft coupled arrays.

We have also described the hardware development and control experiments that were carried out to demonstrate the accuracy and effectiveness of the dynamics modeling, decentralized under-actuated control, and relative sensing introduced in this paper. A great deal of effort has been concentrated on the development of the new tethered formation flying test bed using the SPHERES nanosatellites. The newly developed hardware includes a reaction-wheel air-carriage which provides substantially more torque than the thrusters of SPHERES. In particular, the new relative sensing mechanism, using a 6 DOF force-torque sensor and gyroscope, was devised and validated in the closed-loop control experiments. Using the gain-scheduled LQR control law, we successfully demonstrated that a planar rotating array of tethered spacecraft could control all relevant degrees of freedom using only one reaction wheel in each spacecraft. The experimental videos described in this paper can be downloaded at http://ssl.mit.edu/spheres/videos.html.

Acknowledgments

The authors gratefully acknowledge the NASA Goddard Space Flight Center (Contract Monitor, David Leisawitz) for both financial and technical support for the Massachusetts Institute of Technology Space Systems Laboratory and Payload Systems Synchronized Position Hold, Engage, and Reorient Experimental Satellites Tether program. The authors would like to thank the associate editor (Jesse Leitner) and the anonymous reviewers for their truly constructive feedback. The authors also thank Danielle Adams, Alvar Saenz-Otero, John Merk, Edmund Kong, and Christophe Mandy for the technical discussions and support. The hardware described in this paper has been developed in collaboration with Payload Systems, Inc.

References

[1] Harwit, M., Leisawitz, D., Rinehart, S., Benford, D., Budinoff, J., Chalmers, R., Cottingham, C., Danchi, W., DiPirro, M. J., Farley, R., Hyde, T. T., Jones, A. L., Kuchner, M. J., Liu, A., Lyon, R., Mather, J. C., Marx, C. T., Martino, A. J., Moseley, S. H., Ollendorf, S., Quinn, D. A., Silverberg, R. F., Whitehouse, P., Wilson, M., Pearson, J. C., Lawrence, C., Serabyn, E., Shao, M., Smythe, R., Yorke, H. W., Mundy, L. G., Lorenzini, E., Bombardelli, C., Allen, R. J., Calcetti, D., Blain, A., Doggett, W., Labeyrie, A., Nakagawa, T., Neufeld, D. A., Satyapal, S., Stacey, G., Wright, E. L., Elias, N. M., Fischer, D., Leitch,

J., Noecker, M. C., Espero, T., Friedman, E. J., Woodruff, R. A., and Lillie, C., "Kilometer-Baseline Far-Infrared/Submillimeter Interferometer in Space," Submillimeter Probe of the Evolution of Cosmic Structure Vision Mission Study Final Rept., AIAA (submitted for publication), 2008.

[2] Quinn, D. A., and Folta, D. C., "Tethered Formation Flying Concept for the SPECS Mission," *Proceedings of the 23rd Rocky Mountain Guidance and Control Conference*, Vol. 104, Univelt, San Diego, CA, 2000, pp. 183–196.

[3] Leisawitz, D. T., Danchi, W. C., DiPirro, M. J., Feinberg, L. D., Gezari, D. Y., Hagopian, M., Langer, W. D., Mather, J. C., Moseley, S. H., Shao, M., Silverberg, R. F., Staguhn, J., Swain, M. R., Yorke, H. W., and Zhang, X., "Scientific Motivation and Technology Requirements for the SPIRIT and SPECS Far-infrared/Submillimeter Space Interferometers," *Proceedings SPIE 4013*, Society of Photo-Optical Instrumentation Engineers, Bellingam, WA, 2000, p. 36.

[4] Farley, R. E., and Quinn, D. A., "Tethered Formation Configurations: Meeting the Scientific Objectives of Large Aperture and Interferometric Science," AIAA 2001-4770, 2001.

[5] Lorenzini, E., Harwit, M., Bombardelli, C., Miller, D., Farley, R., Leisawitz, D., Rinehart, S., "Role of Tethers in Far-Infrared/Submillimeter Astronomical Interferometry from Space," *Astrophysics and Space Science*, Vol. 302, Nos. 1–4, 2006, pp. 225–239. doi:10.1007/s10509-006-9038-7

[6] Chung, S.-J., Miller, D. W., and deWeck, O. L., "ARGOS Testbed: Study of Multidisciplinary Challenges of Future Spaceborne Interferometric Arrays," *Optical Engineering*, Vol. 43, No. 9, Sept. 2004, pp. 2156–2167. doi:10.1117/1.1779232

[7] Chung, S.-J., "Nonlinear Control and Synchronization of Multiple Lagrangian Systems with Application to Tethered Formation Flight Spacecraft," Sc.D. Thesis, Dept. of Aeronautics and Astronautics, Massachusetts Inst. of Technology, Cambridge, MA, 2007.

[8] Chung, S.-J., Slotine, J.-J. E., and Miller, D. W., "Nonlinear Model Reduction and Decentralized Control of Tethered Formation Flight," *Journal of Guidance, Control, and Dynamics*, Vol. 30, No. 2, 2007, pp. 390–400. doi:10.2514/1.21492

[9] Kumar, K. D., "Review of Dynamics and Control of Non-electrodynamic Tethered Satellite Systems," *Journal of Spacecraft and Rockets*, Vol. 43, No. 4, July–Aug. 2006, pp. 705–720.

[10] Levin, E. M., *Dynamics Analysis of Space Tether Missions, Advances in the Astronautical Sciences*, Vol. 126, American Astronautical Society, San Diego, CA, 2007.

[11] DeCou, A. B., "Tether Static Shape for Rotating Multimass, Multitether, Spacecraft for Triangle Michelson Interferometer," *Journal of Guidance, Control, and Dynamics*, Vol. 2, No. 2, March 1989, pp. 273–275.

[12] Kim, M., and Hall, C. D., "Control of a Rotating Variable-Length Tethered System," *Journal of Guidance, Control, and Dynamics*, Vol. 27, No. 5, Sept.–Oct. 2004, pp. 849–858.

[13] Bombardelli, C., Lorenzini, E. C., and Quadrelli, M. B., "Retargeting Dynamics of a Linear Tethered Interferometer," *Journal of Guidance, Control, and Dynamics*, Vol. 27, No. 6, Nov–Dec 2004, pp. 1061–1067.

[14] Bombardelli, C., Lorenzini, E. C., and Quadrelli, M. B., "Formation Pointing Dynamics of Tether-Connected Architecture for Space Interferometry," *Journal of the Astronautical Sciences*, Vol. 52, No. 4, Oct.–Dec. 2004, pp. 475–493.

[15] Quadrelli, M. B., "Modeling and Dynamics Analysis of Tethered Formations for Space Interferometry," American Astronautical Society Paper 01-231, 2001.

[16] Misra, A. K., "Equilibrium Configurations of Tethered Three-Body Systems and Their Stability," American Astronautical Society Paper 01-191, 2001.

[17] Cosmo, M., and Lorenzini, E. M., *Tethers in Space Handbook*, 3rd ed., prepared for NASA Marshall Space Flight Center by Smithsonian Astrophysical Observatory, Cambridge, MA, 1997.

[18] Gwaltney, D. A., and Greene, M. E., "Ground-Based Implementation and Verification of Control Laws for Tethered Satellites," *Journal of Guidance, Control, and Dynamics*, Vol. 15, No. 1, 1992, pp. 271–273.

[19] Bernelli-Zazzera, F., "Active Control of Tether Satellites via Boom Rotation: A Proof of Concept Experiment," *Advances in the Astronautical Sciences*, Vol. 108, Pt. 2, 2001, pp. 1225–1240.

[20] Wilson, J. M., "Control of a Tethered Artificial Gravity Spacecraft," Ph.D. Thesis, Stanford Univ., 1990.

[21] Saeed, S. I., "Optimal Control of Tethered Artificial Gravity Spacecraft," Ph.D. Thesis, Stanford Univ., Palo Alto, CA, March 1997.

[22] Kline-Schoder, R., and Powell, J. D., "Recent Laboratory Results of the KITE Attitude Dynamics Simulator," *Proceedings of 2nd International Conference on Tethers in Space*, edited by L. Gnerriero and I. Bekey, Washington, D.C., 1987, pp. 61–66.

[23] Nakaya, K., Lai, M., Omagari, K., Yabe, H., and Matunaga, S., "Formation Deployment Control for Spinning Tethered Formation Flying: Simulations and Ground Experiments," *AIAA Guidance, Navigation, and Control Conference*, AIAA Paper 2004-4896, Aug. 2004.

[24] Nakaya, K., and Matunaga, S., "On Attitude Maneuver of Spinning Tethered Formation Flying Based on Virtual Structure Method," *AIAA Guidance, Navigation, and Control Conference*, AIAA Paper 2005-6088, Aug. 2005.

[25] Wie, B., *Space Vehicle Dynamics and Control*, AIAA, Reston, VA, 1998.

[26] Slotine, J.-J. E., and Li, W., *Applied Nonlinear Control*, Prentice–Hall, Upper Saddle River, NJ, 1991.

[27] Olfati-Saber, R., "Nonlinear Control of Underactuated Mechanical Systems with Application to Robotics and Aerospace Vehicles," Ph.D. Thesis, Dept. of Electrical Engineering and Computer Science, Massachusetts Inst. of Technology, Cambridge, MA, Feb. 2001.

[28] Bullo, F., and Lewis, A. D., *Geometric Control of Mechanical Systems: Modeling Analysis, and Design for Simple Mechanical Control Systems*, Texts in Applied Mathematics, Springer–Verlag, Berlin, 2004.

[29] Chung, S.-J., Slotine, J.-J. E., and Miller, D. W., "Propellant-Free Control of Tethered Formation Flight, Part 2: Nonlinear Underactuated Control," *Journal of Guidance, Control, and Dynamics* (submitted 2007).

[30] Rugh, W. J., and Shamma, J. S., "Research on Gain Scheduling," *Automatica*, Vol. 36, No. 10, 2000, pp. 1401–1425. doi:10.1016/S0005-1098(00)00058-3